SUPPORTING INFORMATION

Nanoscale Chemical Imaging of an Individual Catalyst Particle with Soft X-Ray Ptychography

Anna M. Wise[†], *Johanna Nelson Weker*[†], *Sam Kalirai*[§], *Maryam Farmand*[‡], *David A. Shapiro*[‡], *Florian Meirer**[§], *Bert M. Weckhuysen**[§]

† Stanford Synchrotron Radiation Lightsource, Stanford University, Menlo Park, CA 94025, USA.

§ Inorganic Chemistry and Catalysis group, Debye Institute for Nanomaterials Science, Utrecht University, Utrecht, The Netherlands.

‡ Advanced Light Source, Lawrence Berkeley National Laboratory, Berkeley, CA 94720, USA.

Corresponding Authors

* E-mail: f.meirer@uu.nl, b.m.weckhuysen@uu.nl

Sample preparation

Whole individual fluid catalytic cracking (FCC) equilibrium catalyst (ECAT) particles were fixed in a gel cap with Epofix™ resin and allowed to harden overnight in an oven at 60°. The hardened samples were then cut into 500 nm thin sections using an Ultracut E Reichert-Jung microtome (*Leica*) equipped with a glass knife. The samples were collected and placed on to a previously glow-discharged, Formvar coated copper electron microscopy (EM) grid with 50-mesh size.

Ptychography

Ptychography is a coherent diffraction imaging technique in which extended samples can be studied by raster scanning the sample through the incident coherent X-ray beam, recording the far-field diffraction pattern at each sample position. Iterative phase reconstruction algorithms are then employed to reconstruct the complex index of refraction of the material, generating high-resolution images utilizing the phase and absorption contrast. Each sample position overlaps with its neighbor, providing the real-space constraint required to reconstruct the phase.[1,2]

Ptychography data were collected at the bending magnet beamline 5.3.2.1 of the Advanced Light Source, Lawrence Berkeley National Laboratory. Beamline 5.3.2.1 is a scanning transmission X-ray microscope beamline[3] which has been adapted to enable the collection of ptychographic data by the installation of a custom developed high frame rate CCD camera. All data, both scanning transmission X-ray microscopy (STXM) and ptychography, were recorded using a zone plate with 100 nm outer zone width to define a beam size of 100 nm on the sample. STXM data were collected with a dwell time of 5 ms, whereas a 500 ms exposure time was used for the collection of each scattering pattern for ptychography. A step size of 70 nm was used for ptychography to provide sufficient overlap of the sample positions for the reconstruction. Scattering patterns were processed as described previously[4] and data were reconstructed to obtain images with a pixel size of 4.6 nm using the SHARP-CAMERA software package.[5]

Elemental Distribution

Ptychography images recorded over a 7 μm x 7 μm region at the La M_5 and Fe L_3 absorption edges were aligned using the StackReg[6] plugin in ImageJ.[7] The images were converted from absorption intensity to optical density (OD), where the OD is a product of the linear absorption coefficient and the sample thickness. Difference maps were created to identify the location of La and Fe by subtracting the pre-edge image from the post-edge image (710 eV – 704 eV to isolate Fe, 834.5 eV – 830 eV for La). The difference maps were then combined to create the La and Fe distribution map using the RGBT_PhaseMap feature in TXMWizard.[8]

Image Resolution

The resolution of the reconstructed ptychography images was estimated by fitting a Gaussian curve to a lineout across a high contrast feature. The full width at half maximum (FWHM) of the Gaussian fit was taken as the resolution. Because the image of a feature is the convolution of the imaging point spread function with the feature, this method of determining the resolution is very conservative and the true imaging resolution could be much smaller. Since the resolution is dependent on the energy, an estimate was calculated at the La edge (**Figure S1**) and the Fe edge (**Figure S2**). The resolution at the La edge is estimated to be 12. 6 nm and 12.5 nm at the Fe edge.

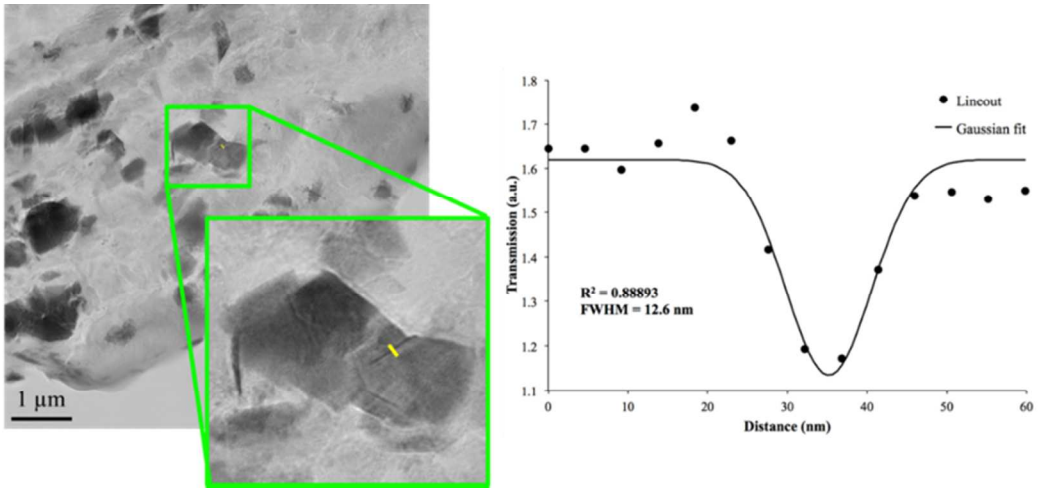

Figure S1. Resolution at the La edge (834.5 eV) is estimated to be 12.6 nm or better. It was calculated fitting a Gaussian curve (right) to a lineout (left, yellow line) across a high contrast feature.

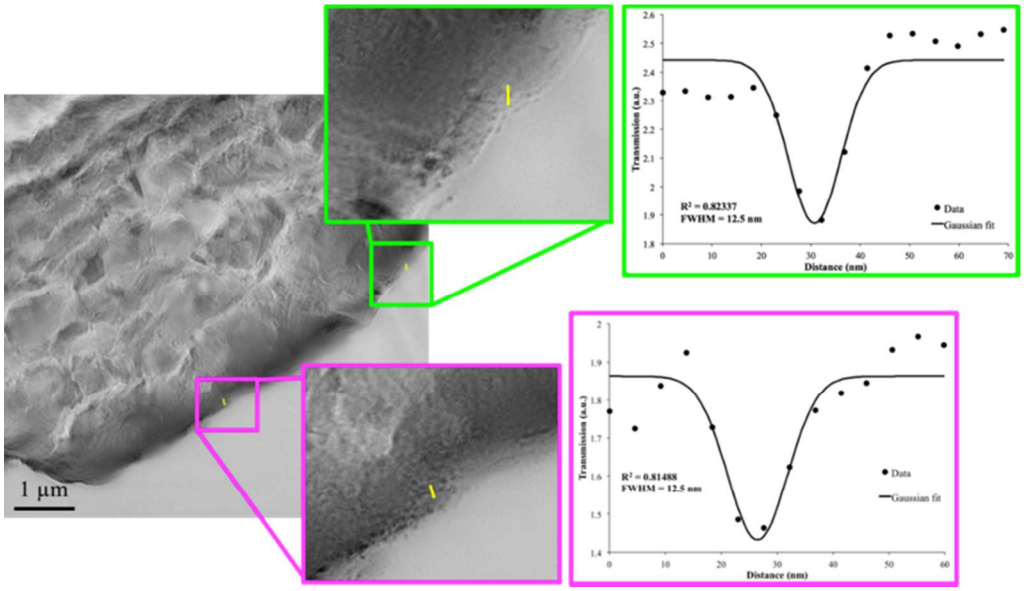

Figure S2. Resolution at the Fe edge (710 eV) is estimated to be 12.5 nm or better. It was calculated fitting Gaussian curves (right) to lineouts (left, yellow line) across two different high contrast features.

An alternative method of estimating the imaging resolution employs the Fourier ring correlation (FRC), also called spatial frequency correlation function. Here the normalized cross-correlation coefficient between two 2D images is calculated. The two images were reconstructed from two independent datasets by taking data from every other column.[9] Since only half the data is used for each independent reconstruction, the overlap between data spots is reduced. Thus the quality of the two reconstructed images is lower. Determining the cutoff frequency to establish the imaging resolution is rather arbitrary; however, we have chosen halfway between the 0.5 and half-bit thresholds. This gives a spatial resolution of 12.2 nm at the La edge (**Figure S3**) and 14.2 nm at the Fe edge (**Figure S4**), which are in good agreement with the previous resolution estimates.

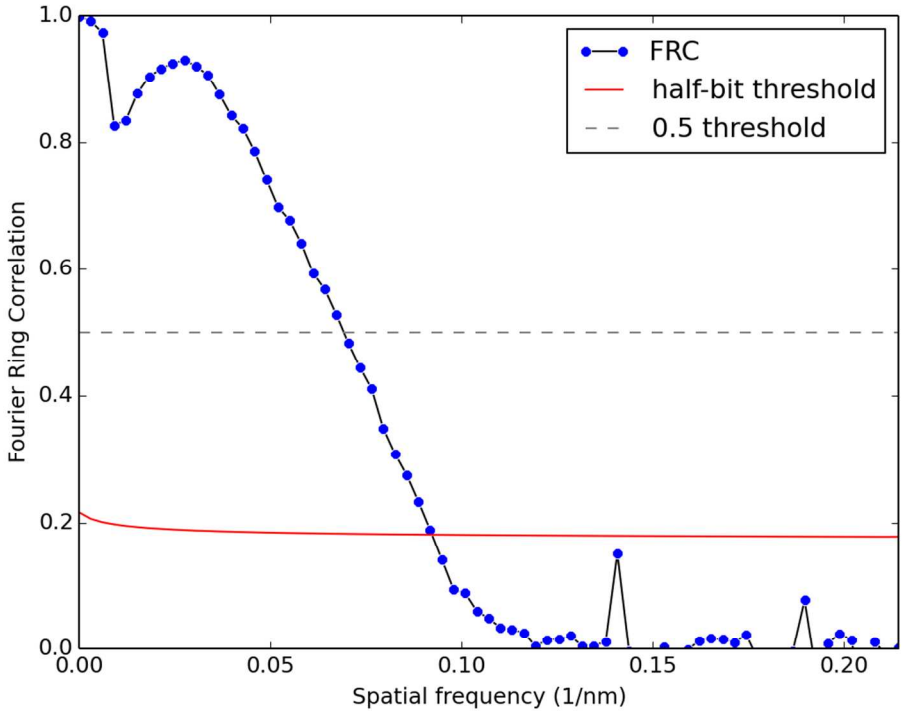

Figure S3. Plot of the Fourier ring correlation function at the La edge (834.5 eV). If the cutoff frequency is chosen to be halfway between the 0.5 and half-bit threshold, the estimated resolution is 12.2 nm.

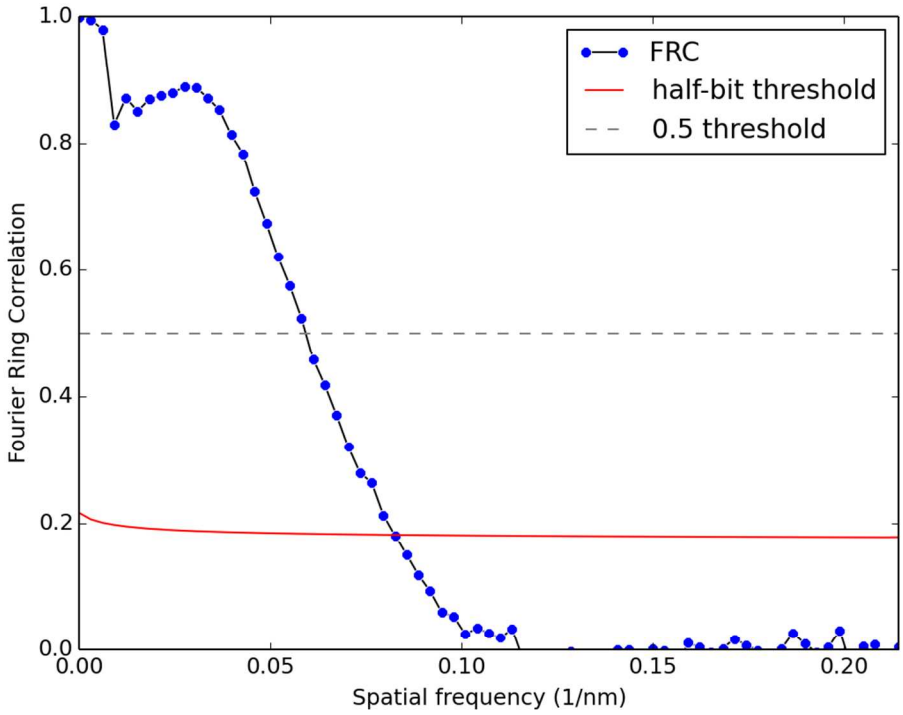

Figure S4. Plot of the Fourier ring correlation function at the Fe edge (710 eV). If the cutoff frequency is chosen to be halfway between the 0.5 and half-bit threshold, the estimated resolution is 14.2 nm.

La Domain Size Analysis

Figure S5 shows the La M_5 edge map with each zeolite domains visible. Green markers are overlaid to indicate the centroid, or geometrical center of the zeolite domains. The unique domains were determined by performing a watershed algorithm on the masked La edge map. The result from the watershed algorithm was further refined manually to concatenate zones that were over-segmented.

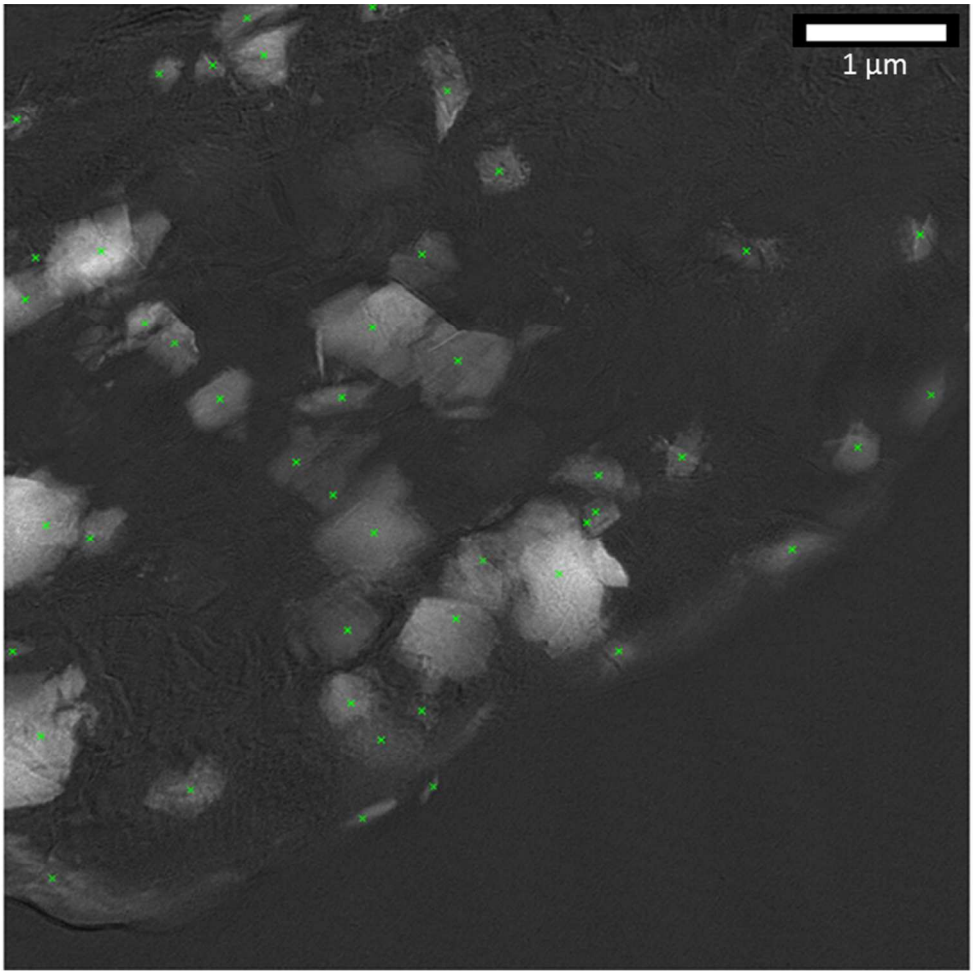

Figure S5. La zeolite domains with green markers indicating the centroid of the domains.

Fe L_3 NEXAFS Data Processing

Intensity stacks at the Fe L_3 edge were aligned using the aXis 2000 software package. Alignment was performed iteratively using a Fourier transform cross-correlation algorithm in order to align each preceding image in the stack until the resulting alignment correction was at the sub-pixel level. The images were converted from absorption intensity (A) in to optical density (OD), where the OD is a product of the linear absorption coefficient and the sample thickness.

Principle Component Analysis and Clustering of the Spectromicroscopic Data Set

To study possible differences in Fe chemical states and their spatial distribution we performed principal component analysis (PCA) and subsequent clustering.[10-13] The recorded data set consisted of 41 images (41 energies) of 436 x 488 pixels. The data matrix therefore contained 212768 single pixel X-ray absorption spectra consisting of 41 energy points, i.e. every pixel represents a data point in 41-dimensional space.

In the first step, to minimize any influence of differences in the average intensity of the pre-edge region on PCA and clustering, a simple offset correction was applied to each single pixel NEXAFS. In this procedure, the average pre-edge intensity in the energy interval 700.0 eV to 704.0 eV was determined and subtracted from each NEXAFS individually.

In the second step, to remove spectra showing no or very low relative Fe concentrations (i.e. absorption edge-jumps), the data set was filtered using the relative Fe concentration map (the Fe edge jump map, **Figure S6a**). The relative Fe concentration map was determined by integrating the recorded X-ray intensities in the energy interval from 707.3 eV to 711.3 eV. Then pixels with

integrated intensities of smaller or equal to zero were removed. (Negative values originated from the offset correction performed in step 1).

In the third step PCA[14,15] using singular value decomposition (SVD) of the offset corrected, filtered, and mean centered data matrix A was employed to reduce the data set from 41 to 3 dimensions, using the first 3 principal components (PCs). This can be done without losing significant information because the first few principal components explain most of the data's variance. For SVD the so called economy sized decomposition was used, saving both calculation time and computer storage by calculating only the first E columns of U and producing the same matrix V but the matrix S with reduced dimensions E x E:

'regular' SVD: $$A_{p\,x\,E} = U_{p\,x\,p} \cdot S_{p\,x\,E} \cdot V^{T}_{E\,x\,E} \quad [1]$$

'economy sized' SVD: $$A_{p\,x\,E} = U_{p\,x\,E} \cdot S_{E\,x\,E} \cdot V^{T}_{E\,x\,E} \quad [2]$$

where the indices p and E indicate number of pixels and energies respectively.

Here, the matrix U has orthogonal columns, the matrix V has orthonormal rows, and the matrix S is a diagonal matrix containing the singular values. When using SVD for PCA, the eigenvalues of the data matrix A are given by $\lambda_{1..E} = S^2$, and the eigenvectors are the columns of V. When working with spectroscopic image data these eigenvectors are commonly called eigenspectra. Correspondingly, the columns of U can be reshaped into images and are called eigenimages.

In our case, the first 3 PCs explained more than 81% of the cumulative variance in the data (Figure S4a). The choice of using the first 3 PCs was further based on the inspection of the eigenspectra and eigenimages (**Figure S6b, c**), which showed that only the first two eigenimages showed spatial pattern with significant intensities. Correspondingly, eigenspectra above the 3rd PC contained mainly noise and were therefore not used for clustering. As a result each data point (pixel) was described by 3 PCs (parameters), i.e. projected to 3-dimensional principal component

space (called ‘score plot’ in the following). Because the PCs are oriented to best describe the spread in the data this projection highlights the pattern explained by the captured variance and effectively reduces noise, which is described by PCs having indices larger than 3. The distance between data points in the score plot is a direct measure of the similarity of the NEXAFS, i.e. the chemical phase, and can be used to cluster pixels according to their (Euclidean) distances from cluster centers, for example by using the centroid linkage method for k-means clustering.[16,17] Such clustering therefore results in an image segmentation into k regions of similar NEXAFS, i.e. Fe chemical state.

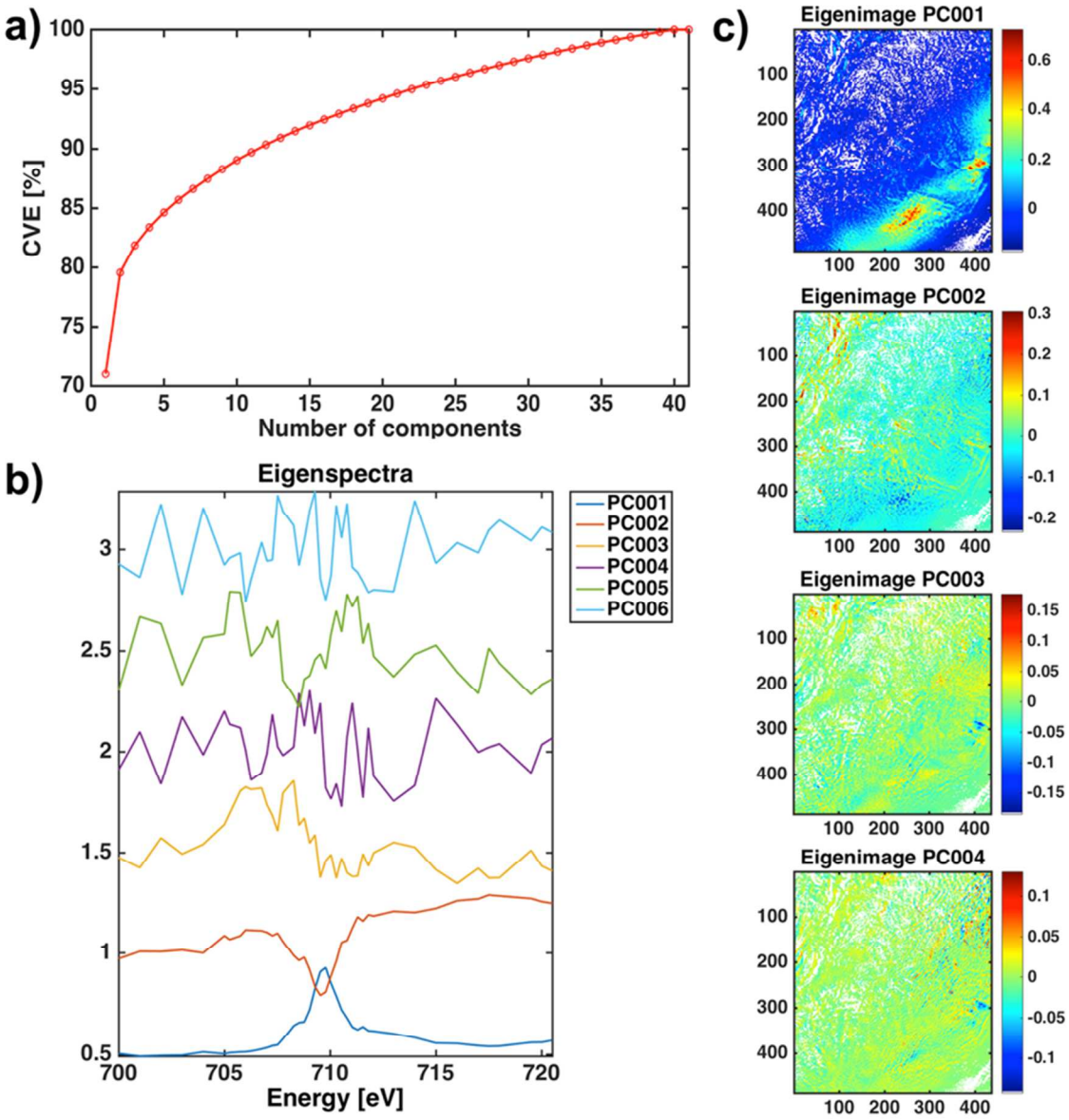

Figure S6. Principal component analysis of the spectromicroscopic data set. In (a) the percent cumulative variance explained (CVE) is plotted for all 41 principal components (PC). Panel (b) shows the first 6 eigenspectra and panel (c) reports the first 4 eigenimages after PCA.

In k-means clustering the number of clusters k has to be assigned manually and has to be equal or larger to the number of PCs used (here 3). However, in order to exploit all the information provided by the reduced PC space, the data was, in the fourth step, intentionally over-clustered using k = 6. This typically results in a more sensitive image segmentation that is able to capture gradual changes in chemistry, i.e. phase gradients in the sample. The result of the image segmentation by k-means clustering is reported in **Figure S7a**. It is obvious from the segmented score plot (**Figure S7b**) that k-means clustering is not able to effectively segment areas of different point density in the score plot. Cluster 2 (red), for example, contains pixels of very low Fe concentrations, which are expected to be located mainly in the lower right corner of the image, i.e. outside the sample. However, this cluster also contains many pixels located in the body of the particle, and the average NEXAFS of this cluster (**Figure S7c**) shows that these pixels still produce a weak but appreciable signal.

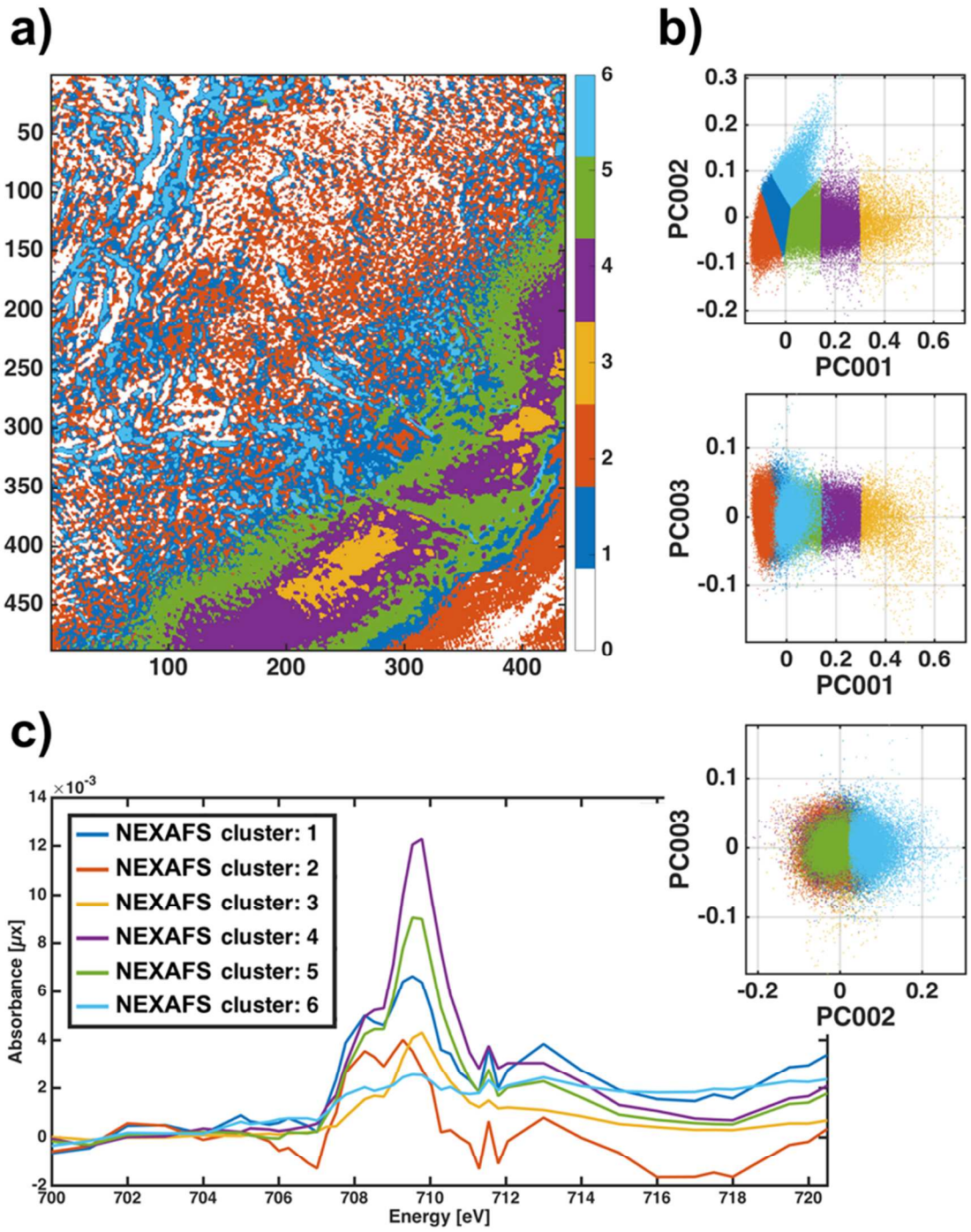

Figure S7. Result of k-means clustering in PC space. Panel (a) reports the resulting image segmentation based on the k-means clustering of the score plot using 6 clusters (b). In (c) the average NEXAFS of each cluster is plotted, showing significant differences in the Fe chemical state of different clusters.

In the fifth and final step, in order to improve the k-means clustering, we therefore performed a density based clustering of the reduced data set using the k-means result as an initial guess for a Gaussian Mixture Model (GMM) and employing an expectation-maximization (EM) algorithm to iteratively refine the solution.[18] The result of this clustering refinement provides the same number of clusters but is based on the point density in PC space (i.e. in the score plot). Furthermore, because the distribution is now described by set of overlapping Gaussians, each data point (pixel) is assigned a class membership value, indicating the degree (or weight) to which it belongs to a certain cluster. The latter is especially useful when calculating the (now weighted) average NEXAFS of each cluster, where this class membership value can be used as a weight for each pixel, determining how much each pixel contributes to the average NEXAFS of the cluster.

The result of the GMM clustering refinement is reported in **Figure S8**. It is clear from both the segmentation of the score plot and the image that this approach improved the segmentation significantly.

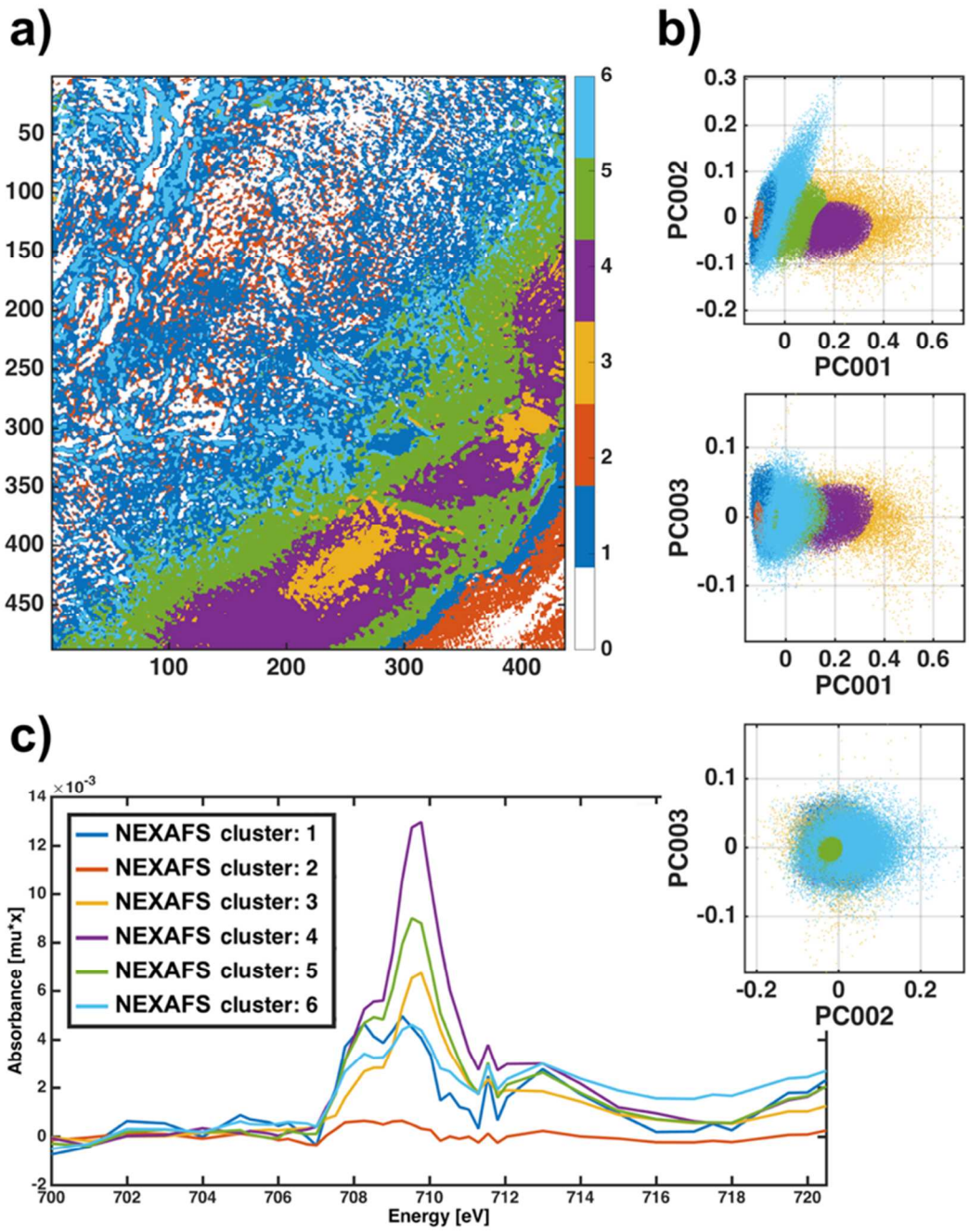

Figure S8. Result of density based clustering in PC space. Panel (a) reports the final image segmentation based on the density based clustering of the score plot (b) using a Gaussian Mixture Model (GMM) and the k-means clustering reported in **Figure S7** as initial guess. In (c) the weighted average NEXAFS of each cluster is plotted, using the class membership values obtained from GMM as weights.

Linear Combination Fitting

To estimate the amount of Fe^{2+} and Fe^{3+} present in the FCC particle sample, a linear least squares fit at each pixel in the Fe L_3 image stack (700 – 716.9 eV) was performed. Reference spectra for FeO and Fe_2O_3 [19] were used to estimate the ratio of Fe^{2+} and Fe^{3+} in each pixel by minimizing the difference between the left-hand side and right-hand side of the equation at each pixel (*i, j*):

$$G(i, j) = a_0(i, j) + \Sigma_n\, a_n(i, j) \times G_n \qquad [1]$$

Where $G(i, j)$ the raw intensity at each pixel, a_i is the effective thickness of the reference spectrum G_n and a_0 is a constant background.

The results of the LCF were used to generate maps of Fe^{2+} and Fe^{3+} intensity (Figure 5, A and B), which were rescaled and combined to create the phase map (Figure 5C) showing the distribution of Fe species. The quality of the fit at each pixel was assessed using an R-squared value, with 1 corresponding to a perfect fit. The resulting map of R-squared values is shown in **Figure S9**. As can be seen from the map, the goodness-of-fit decreases towards the center of the particle – this is due to the lower concentration of Fe present in this region. The spectra of pixels identified as predominantly Fe^{2+} or Fe^{3+} are shown in **Figure S10**, along with the FeO and Fe_2O_3 reference spectra, with good agreement seen between peak positions.

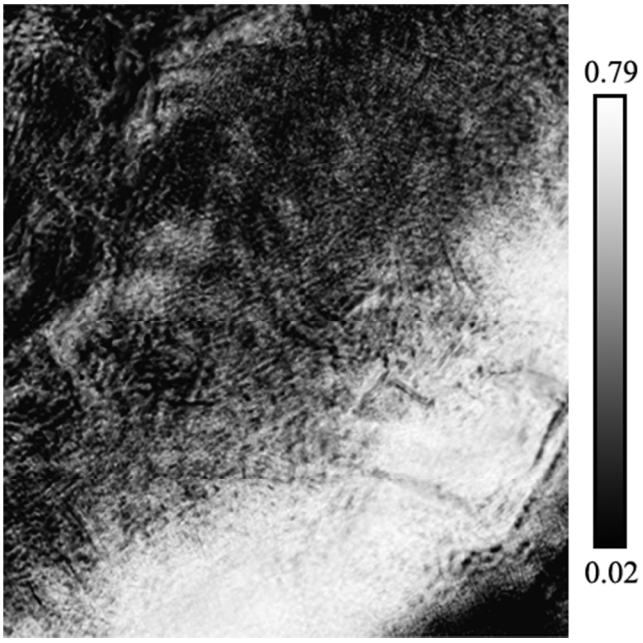

Figure S9. Map of R-squared values relating to the goodness-of-fit of the linear combination fitting of Fe species.

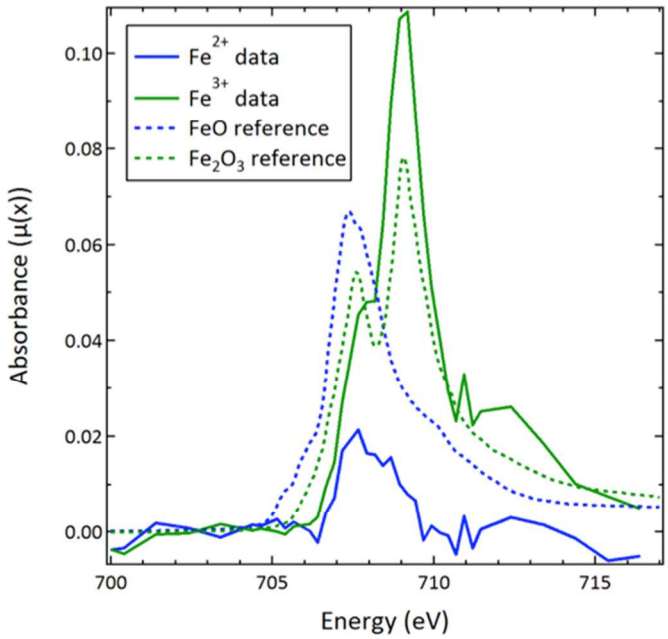

Figure S10. NEXAFS spectra from pixels identified as predominantly Fe^{2+} or Fe^{3+} compared with the FeO and Fe_2O_3 reference spectra.

References:

(1) Thibault, P.; Dierolf, M.; Menzel, A.; Bunk, O.; David, C.; Pfeiffer, F. *Science* **2008**, 321, 379-382.

(2) Rodenburg, J. M.; Hurst, A. C.; Cullis, A. G.; Dobson, B. R.; Pfeiffer, F.; Bunk, O.; David, C.; Jefimovs, K.; Johnson, I.; *Phys. Rev. Lett.* **2007**, 98, 034801, 1-4.

(3) Kilcoyne, A. L. D.; Tyliszczak, T.; Steele, W. F.; Fakra, S.; Hitchcock, P.; Franck, K.; Anderson, E.; Harteneck, B.; Rightor, E. G.; Mitchell, G. E.; Hitchcock, A. P.; Yang, L.; Warwick, T.; Ade, H. *J. Synchrotron Radiat.* **2003**, 10, 125-136.

(4) Shapiro, D. A.; Yu, Y.-S.; Tyliszczak, T.; Cabana, J.; Celestre, R.; Chao, W.; Kaznatcheev, K.; Kilcoyne, A. L. D.; Maia, F.; Marchesini, S.; Meng, Y. S.; Warwick, T.; Yang, L. L.; Padmore, H. A. *Nat. Photonics* **2014**, 8, 765-769.

(5) Marchesini, S.; Schirotzek, A.; Yang, C.; Wu, H.-t.; Maia, F. *Inverse Probl.* **2013**, 29, 115009.

(6) Thevenaz, P.; Ruttimann, U. E.; Unser, M. *IEEE Trans. Image Process.* **1998**, 7, 27-41.

(7) Schneider, C. A.; Rasband, W. S.; Eliceiri, K. W. *Nat. Meth.* **2012**, 9, 671-675.

(8) Liu, Y.; Meirer, F.; Williams, P. A.; Wang, J.; Andrews, J. C.; Pianetta, P. *J. Synchrotron Radiat.* **2012**, 19, 281-287.

(9) Deng, J.; Vine, D. J.; Chen, S.; Nashed, Y. S. G.; Jin, Q.; Phillips, N. W.; Peterka, T.; Ross, R.; Vogt, S.; Jacobsen, C. J. *Proc. Natl. Acad. Sci.* **2015**, 112, 2314-2319.

(10) Lerotic, M.; Jacobsen, C.; Schäfer, T.; Vogt, S.; *Ultramicroscopy* **2004**, 100, 35-57.

(11) Boesenberg, U.; Meirer, F.; Liu, Y. J.; Shukla, A. K.; Dell'Anna, R.; Tyliszczak, T.; Chen, G. Y.; Andrews, J. C.; Richardson, T. J.; Kostecki, R.; Cabana, J. *Chem. Mater.* **2013**, 25, 1664–1672.

(12) Meirer, F.; Liu, Y.; Pouyet, E.; Fayard, B.; Cotte, M.; Sanchez, C.; Andrews, J. C.; Mehta, A.; Sciau, P. *J. Anal. At. Spectrom.* **2013**, 28, 1870–1883.

(13) Lerotic, M.; Mak, R.; Wirick, S.; Meirer, F.; Jacobsen, C. *J. Synchrotron Radiat.* **2014**, 21, 1206-1212.

(14) Joliffe, I. T. *Principal Component Analysis*, 2nd ed.; Springer-Verlag: New York, 2002.

(15) Jackson, J. E. *A User's Guide to Principal Components;* Wiley: Chichester, 2004.

(16) MacQueen, J. B. *Some Methods for Classification and Analysis of Multivariate Observations*, Proc. Fifth Berkeley Symp. on Math. Statist. and Prob., Univ. of Calif. Press **1967**, 1, 281-297.

(17) Johnson R. A.;Wichern, D. W. *Applied Multivariate Statistical Analysis*, 5th ed.; Pearson: Upper Saddle River, NJ, 2002.

(18) Bishop, C. *Pattern Recognition and Machine Learning*; Springer-Verlag: New York, 2006.

(19) Regan, T. J.; Ohldag, H.; Stamm, C.; Nolting, F.; Lüning, J.; Stöhr, J.; White, R. L. *Phys. Rev. B* **2001**, 64, 214422.